Model Based Multiscale Analysis of Film Formation in Lithium-Ion Batteries

Fridolin Röder,[a, b] Vincent Laue,[a, b] and Ulrike Krewer*[a, b]

Evidence for multiscale interaction of processes during surface film growth is provided using a multiscale modeling approach. The model directly couples a continuum pseudo two dimensional (P2D) battery model and a heterogeneous surface film growth model based on the kinetic Monte Carlo (kMC) method. Key parameters have been identified at basic electrochemical experiments, i.e., open circuit potential (OCP), C-rate tests, and potential during filmformation. Simulations are in very good agreement with these experiments. Simulation results are shown for various formation procedures, i.e., for different applied C-rates. Interaction between macroscopic transport processes on electrode scale and elementary reaction steps on atomistic scale are observed. Results reveal a distinct impact of the applied procedures on the atomistic structure of surface films. It can be seen that locally heterogeneous films are formed with very slow charging rate due to stochasticity of the growth process, while spatially heterogeneous films are formed with very fast charging rate due to the spatial heterogeneous distribution of concentration and potential. Therefore, the author's emphasize that in order to identify charging protocols for optimal film morphology multiscale interactions should be considered.

1. Introduction

Lithium-ion batteries play a major role in enabling the energy market to move from fossil fuels to renewable energy sources. This holds in particular for electromobility. In order to achieve consumer acceptance, there is a need to reduce cost, ensure safety, and provide long life times. These targets are often related to unwanted side reactions and surface film growth at electrochemical active surfaces within porous electrodes. Detailed model based analysis of the final production step during lithium-ion battery production, namely the formation of a stable solid electrolyte interface (SEI) film at the negative electrode during the first cycles will enable one to optimize this step to achieve a shorter formation time, i.e., reduced production cost, and more stable films, i.e., increased life time, capacity, and safety.

In general, the chemical and microstructural properties of the SEI depend on graphite structure, electrolyte composition, temperature and electrochemical conditions, e.g., cut-off-potential and current densities,[1] which has been shown in many experimental investigations. Märkle et al.[2] showed experimentally using post mortem scanning electron microscopy that film morphology can be controlled by the current in the first cycle and has considerable impact on the cycling stability of the cell. The impact of temperature and upper cut-off-voltage has been shown by German et al.[3] Further, Antono-poulos et al.[4] carried out formation experiments with constant potential and demonstrated a significant impact on the chemical composition of the SEI as well as the performance of the cell after formation. The microstructure of the SEI has a significant impact on the cell performance.[5] It has been demonstrated that the SEI can have a non-homogeneous structure, consisting of several SEI microphases.[6,7] Chattopad-hyay et al.[8] experimentally observed LiF crystals within the SEI and suggest that their orientation may influence Li^+ diffusion and thus performance of the battery. The formation of clusters have been also observed by molecular dynamic (MD) simulations.[9] As degradation and cell failure is often triggered by heterogeneity on nano- and mesoscale,[10,11] it is essential to study and understand its origin in order to achieve optimal battery performance.

Within the last decade numerous model based investigations have been published, which study SEI formation, aging, reaction mechanisms, transport phenomena and morphology. In the following, we briefly elaborate on those as well as the novelty and scope of this paper.

Degradation reaction mechanisms for the decomposition of ethylene carbonate (EC) were implemented by Safari et al.[12] and Colcasure et al.[13] These continuum models enable to study complex reaction networks, film growth and capacity fade, but do not consider reaction heterogeneity such as the aforementioned crystal growth[8] or cluster formation.[9] Heterogeneous reaction mechanisms can be simulated on atomistic scale using MD[9] or kinetic Monte Carlo (kMC) methods,[14,15] for example. Molecular simulations are widely used to study certain degradation reactions in solutions or on surfaces of electrodes,[16–19] but it is difficult to model full cycles with MD, as such simulations cover rather ms than several minutes. Moreover, MD and kMC models do not consider spatial distribution and time dependency of species concentration and potential. In contrast, continuum models have been used to simulate spatial distribu-

[a] F. Röder, V. Laue, Prof. Dr. Ing. U. Krewer
     Institute of Energy and Process Systems Engineering, TU Braunschweig,
     Franz Liszt Strasse 35, 38106 Braunschweig, Germany
     E mail: u.krewer@tu braunschweig.de
[b] F. Röder, V. Laue, Prof. Dr. Ing. U. Krewer
     Battery LabFactory Braunschweig, TU Braunschweig Langer, Kamp 8, 38106
     Braunschweig, Germany

tion of the SEI thickness due to cycling aging[20,21] and for evaluation of statistical distributions using population balance equations.[22] In these aging studies no significant distribution of thickness has been observed. Since film properties have been assumed to be homogeneous and no morphological or structural aspects have been considered, thickness tends to equilibrate and spatial differences are only visible under extreme conditions, e.g., high currents or thick electrodes. Transport processes and growth limiting steps have been studied frequently with model based approaches[23,24] and strongly depend on the actual film morphology and molecular structure as will be discussed in more detail below. To conclude, single scale models presently do not enable simulation of the molecular buildup for long time scales in order to evaluate heterogeneity and spatial distribution of structural properties.

Coupling of continuum models with less detailed molecular simulations provides a feasible and promising way to cover and bridge long time and length scales. This can be achieved by adequate multiscale techniques[25] as has been demonstrated for several related electrochemical problems.[26,27] In our previous work we established the required methodology by detailed investigation of numerical implementations[28] and by demonstration for heterogeneous EC reduction within a continuum single particle model.[29] A similar multiscale model has been introduced by Shinagawa et al.[30] to study film growth and capacity fade of a battery. However, in these models, macroscopic transport processes, e.g., charge and mass transport processes inside the electrode, were lumped, with only diffusion in particles being discretised. This assumption limits the application to slow formation procedures. Thus, previous investigations could not reveal distinct multiscale interactions, which enable to explain experimental observations outlined above. A discretised, macroscopically parameterizable multiscale model for formation would allow to model heterogeneous film growth dependent on the spatial position within the electrode.

In this article, we study multiscale interaction for the buildup of the surface film. Beyond the state of the art, this includes the impact of the applied current on spatial and statistical distribution of the film structure on molecular scale. Parameters of macroscopic processes are identified using electrochemical experiments. Lumped hypothetical mechanisms on the molecular scale are introduced, while rate expressions are derived from macroscopic reversible thermodynamic and kinetic expressions. This enables the identification of key parameters of the atomistic model and a good agreement with the electrochemical experiments.

This article is structured as follows. First the experiments and the model based analysis and parameterization concept is presented. Afterwards, the continuum model and the kMC model are provided, while main parameters of the operational processes and the degradation process are identified, respectively. Based on the parameterized multiscale model, distinct multiscale effects are revealed by studying the first charge of the battery with variation of the applied current.

2. Multiscale Analysis

2.1. Experiments

For experimental characterization, electrodes were produced in the Battery LabFactory Braunschweig. The cell was assembled and characterized in a three electrode setup using the PAT-cell format of the EL-cell company. As active materials, commercial $Li(Ni_{1/3}Co_{1/3}Mn_{1/3})O_2$ and graphite were used as the positive electrode (cathode), and the negative electrode (anode), respectively. Electrodes were produced using carbon black, graphite, binder (PVDF), and the active material in the respective ratio 4:4:2:90, for the cathode and 5:2:2:91, for the anode. The ratio is thereby given in weight-%. Cells were filled with electrolyte using ethylene carbonate (EC), dimethyl carbonate (DMC), and ethyl methyl carbonate (EMC) solvents in the ratio 1:1:1 with 1 M $LiPF_6$ including 2% vinyl carbonate (VC) and 3% cyclohexyl benzene (CHB).

The cell was characterized electrochemically in two regions, during the first formation cycles, where significant contribution of side reactions occur, and after the initial film formation, where no significant contributions of side reactions are expected. The experimental data for formation, open circuit potential and C-rate tests, are used for parameter identification of the electrochemical model. Formation was performed with 2.15 A m^2. OCP was measured by incrementally discharging in steps of 0.05 V. The C-rate test was performed for cell discharge with 4.2, 21.5, and 64.5 A m^2 between 4.2 and 2.9 V. Cells were tested using a potentiostat (VMP3, Biologic, France) at 25 °C.

2. 2. Concept for Model Based Analysis

In this article, multiscale interaction is studied for the lithium-ion battery given above doing a model based analysis of electrochemical measurements. In this section, the multiscale character of the film growth process is outlined with respect to the investigated lithium-ion battery cell. With this in mind, the concept and the scope of the presented model based multiscale analysis are given.

In Figure 1 (A), a lithium-ion battery is illustrated on multiple scales, i.e., electrode scale, particle scale, mesoscale, and atomistic scale. During the charging process under normal operation, i.e., after film formation at the anode, electrons enter the anode. They are conducted through the solid to the active material particle surface, where they electrochemically react at the active material/surface film interface with lithium-ions to form lithium. The lithium then diffuses into the active material host structure. The lithium-ions required for this reaction are produced at the cathode and transported through the electrolyte and the surface film.

Side reactions can take place in a similar manner. As they also consume electrons and lithium-ions at the anode, instead of inserting lithium in the anode host structure, lithium-ions electrochemically react at the particle surface with the solvent components and form a surface film, the SEI. The educts of the electrochemical degradation reaction are electrons, lithium-ions
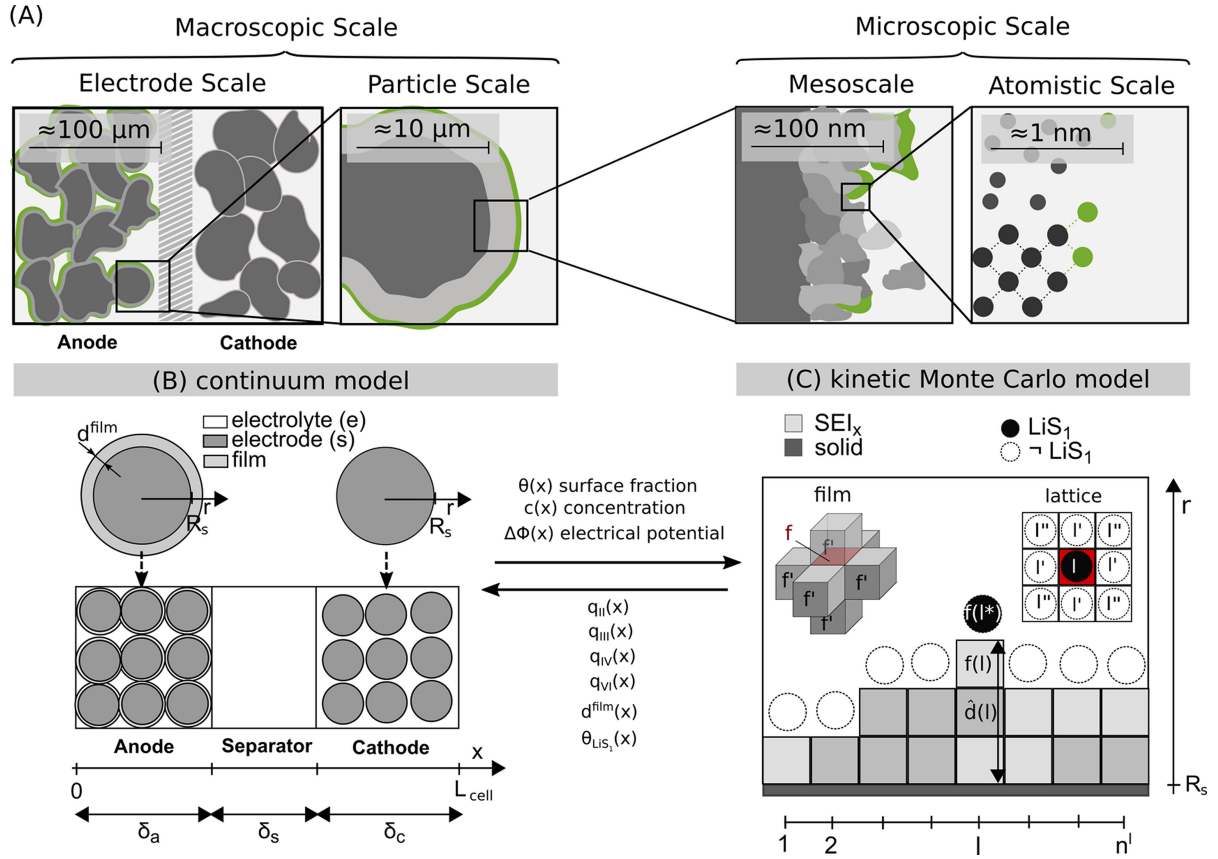
Figure 1. Typical scales within lithium ion battery cell (A), continuum model (B), and kMC model (C).

and solvent components. This requires that either electrons or solvents need to pass through the SEI. Assuming the electrons pass the SEI, the electrochemical degradation reactions take place at the surface film/electrolyte interface. Assuming solvent molecules pass the SEI, degradation reactions take place at the electrode/surface film interface. In either case, the limitations of the electrochemical side reaction process are different from the ones for the normal operation, i.e., charging or discharging, of the battery. Side reactions are always strongly limited by the surface film and are significantly slowed down during buildup. Details on the assumptions applied in this work are given in section 4.1.

The surface film growth is illustrated in Figure 1 (A), marked in green. On the electrode scale, the growth of the surface film will decrease the porosity of the electrode and thus impact diffusion and ion conduction in the electrolyte. On the particle scale, film growth will decrease ion and electron conduction through the film. On the mesoscale, heterogeneous film growth causes blocking or changing of the transport pathways through the film. On an atomistic scale, the surface film/electrolyte interface changes, which has an impact on the lithium-ion transfer between film and electrolyte and the side reactions on the surface film.

Usually, side reactions can barely be detected electrochemically in a single charge/discharge cycle. Because measurements are dominated by the operational processes, their impact can

finally be observed as capacity or power fade in aging experiments. However, at the first charge, i.e., during SEI formation, side reactions are one of the main reaction processes occurring at the anode. This is used in this article by applying a two step parameterization procedure of the model, which is described in the following. First, the operational processes, intercalation, de-intercalation, ion and electron transport in solid and electrolyte are identified using measurements of the open circuit potential and C-rate tests. As these measurements take place after film formation, it is assumed that there is no significant contribution of side reactions to these measurements. In a second step, the parameters of the side reaction process are identified using the first charge cycle of the battery. As parameters of the normal operation after formation have been identified already, a separation of the influence of the side reaction process and thus a separate and more reliable parameter identification is enabled.

All models described in the following sections as well as the model coupling are implemented in MATLAB. Thereby, differential equations are solved using the adaptive solver ode15 s. KMC simulations are always carried out with 9 parallel instances on a 30×30 lattice. Simulations are performed on a single CPU on a desktop PC. Computing time strongly depends on the particular simulation scenario. Here, it has been approximately 10 h computing time per 1 h simulated time for slow formation procedures and and even higher for faster procedures. Calcu-

lation time also strongly depends on the applied coupling algorithms as has been shown previously in.[28]

3. Macroscopic Scale

3.1. Continuum Model

The continuum model is illustrated in Figure 1 (B). The model is based on the P2D model as first proposed by Doyle et al.[31] Additionally, charge balances at electrochemical double layers and a thin film at the particle surface are included based on Legrand et al.[32] and Colcasure et al.,[13] respectively.

The partial and ordinary differential equations are given in Table 1 and cover from top to bottom: mass balance of lithium in solid including diffusion of lithium in the spherical particles, species balance of salt within the electrolyte including diffusion and reaction, balance of dissolved uncharged species in the electrolyte, charge transport in the electrode including diffusion and reaction, charge balance in the electrolyte, charge balance at the electrolrochemical double layer at the solid/surface film (s/film) interface, charge balance at the electrochemical double layer at the adsorption site/electrolyte (ads/e) interface, and the balance of species on the adsorption layer. The time dependent porosity has been taken out of the time derivative, which is a feasible approximation in consideration of slowly changing porosity. The adsorption process of lithium ions from the liquid electrolyte to the surface of the SEI is treated analogously to an electrochemical reaction as suggested by Schleutker et al.[33] Macroscopic and microscopic processes considered at the interfaces are summarized in Table 2. Process I and XI correspond to the normal operation of the battery. Decomposition mechanisms, i.e., Equations 42 45, are included with processes II, III, IV, V, and XII. Further, sorption processes for solvents and

intermediates are included with processes VIII, IX, and X. Surface diffusion processes are given with XII and XIII. In the continuum model, only the macroscopic processes are considered. Processes which are given as microscopic and as macroscopic processes, i.e processes II, III, IV, and VI, are covered by the kMC model, while process fluxes q are synchronized with the continuum model as illustrated in Figure 1. Considered species are given in Table 3, while species covered by the continuum model are indicated accordingly. In the following, details about equations and parameter identification are provided.

The applied current for a 1 C charge is determined as

$$I_{cell}^{1C} = \frac{C_{theo}^{As}}{3600}. \tag{1}$$

The theoretical capacity C_{theo}^{As} is hereby defined as

$$C_{theo}^{As} = c_{max}^a \varepsilon_s^a F \delta_a \tag{2}$$

using the anode thickness δ_a, the anode volume fraction ε_s^a, the maximal concentration in the anode c_{max}^a, and the Faraday constant F. The current density caused by processes at the interfaces is calculated as

$$j_{s,film}^{process} = a_s r_s F(q_I + q_{II} + q_{III} + q_{IV}) \tag{3}$$

for the interface between solid and film and

$$j_{ads,e}^{process} = a_s r_s F(q_{XI}) \tag{4}$$

for the interface between electrolyte and adsorption layer. In these equations, a_s is the specific surface area, r_s is the roughness factor, and q are fluxes according to macroscopic processes given in Table 2. The specific surface area thereby is calculated as the surface area of spherical particles without roughness as

Table 1. Set of partial and ordinary differential equations of the applied P2D continuum battery model with m being the dissolved species in the electrolyte.

Equation	Boundary Condition
$\frac{\partial c_s^{Li}(t,r)}{\partial t} = \frac{1}{r^2}\frac{\partial}{\partial r}\left(D_s^{Li} r^2 \frac{\partial c_s^{Li}(t,r)}{\partial r}\right)$	$\begin{cases} D_s^{Li}\frac{\partial c_s^{Li}(t,0)}{\partial r} = 0 \\ D_s^{Li}\frac{\partial c_s^{Li}(t,R_s)}{\partial r} = r_s q_I(t,x) \end{cases}$
$\varepsilon_e(t,x)\frac{\partial c_e^{salt}(t,x)}{\partial t} = \frac{\partial}{\partial x}\left(D_{e,eff}^{salt}(t,x)\frac{\partial c_e^{salt}(t,x)}{\partial x}\right) + (1 \quad t_p)j_{ads,e}^{process}(t,x)$ $\varepsilon_e(t,x)\frac{\partial c_e^m(t,x)}{\partial t} = \frac{\partial}{\partial x}\left(D_{e,eff}^k(t,x)\frac{\partial c_e^m(t,x)}{\partial x}\right) + a_s r_s q_{ads,e}^m(t,x)$	$\begin{cases} \frac{\partial c_e^{salt}(t,0)}{\partial x} = 0 \\ \frac{\partial c_e^{salt}(t,L_{cell})}{\partial x} = 0 \\ \frac{\partial c_e^m(t,0)}{\partial x} = 0 \\ \frac{\partial c_e^m(t,L_{cell})}{\partial x} = 0 \end{cases}$
$0 = \frac{\partial}{\partial x}\left(\sigma_{s,eff}\frac{\partial \Phi_s(t,x)}{\partial x}\right) + j(t,x)$	$\begin{cases} \sigma_{s,eff}\frac{\partial \Phi_s(t,0)}{\partial x} = I_{cell} \\ \sigma_{s,eff}\frac{\partial \Phi_s(t,\delta_a)}{\partial x} = 0 \\ \sigma_{s,eff}\frac{\partial \Phi_s(t,L_{cell}\;\delta_c)}{\partial x} = 0 \\ \sigma_{s,eff}\frac{\partial \Phi_s(t,L_{cell})}{\partial x} = I_{cell} \end{cases}$
$0 = \frac{\partial}{\partial x}\left(\sigma_{e,eff}(t,x)\frac{\partial \Phi_e(t,x)}{\partial x} \quad \sigma_{De,eff}(t,x)\frac{\partial ln(c_e^{salt}(t,x))}{\partial x}\right) \quad j(t,x)$	$\begin{cases} \Phi_e(t,0) = 0 \\ \frac{\partial \Phi_e(t,L_{cell})}{\partial x} = 0 \end{cases}$
$C_{s,film}^{DL}a_s r_s \frac{\partial \Delta\Phi_{s,film}(t,x)}{\partial t} = j_{s,film}^{DL}(t,x)$ $C_{ads,e}^{DL}a_s r_s \frac{\partial \Delta\Phi_{ads,e}(t,x)}{\partial t} = j_{ads,e}^{DL}(t,x)$ $\frac{N_s}{o_s}\frac{\partial \theta^m(t,x)}{\partial t} = q_{ads}^m(t,x)$	

Table 2. Macroscopic and microscopic processes are considered for lithium de /intercalation, degradation, sorption, and surface diffusion. Processes given as microscopic process are considered by the kMC model, while fluxes are synchronized with the continuum model, displayed as macroscopic processes to the left.

Nb.	Macroscopic Process	j	Microscopic process
I	$V(s) + e^-(s) + Li^+(ads) \rightleftharpoons Li(s) + V(ads)$		
II	$Li^+(ads) + S_1(ads) + e^-(s) \rightleftharpoons LiS_1(ads) + V(ads)$	1	$Li^+(ads) + S_1(ads) + e^-(s) \rightarrow LiS_1(ads) + V(ads)$
		2	$LiS_1(ads) + V(ads) \rightarrow Li^+(ads) + S_1(ads) + e^-(s)$
III	$Li^+(ads) + S_2(ads) + e^-(s) \rightleftharpoons SEI_2(film) + 2V(ads)$	3	$Li^+(ads) + S_2(ads) + e^-(s) \rightarrow SEI_2(film) + 2V(ads)$
		4	$SEI_2(film) + 2V(ads) \rightarrow Li^+(ads) + S_2(ads) + e^-(s)$
IV	$Li^+(ads) + S_3(ads) + e^-(s) \rightleftharpoons SEI_3(film) + 2V(ads)$	5	$Li^+(ads) + S_3(ads) + e^-(s) \rightarrow SEI_3(film) + 2V(ads)$
		6	$SEI_3(film) + 2V(ads) \rightarrow Li^+(ads) + S_3(ads) + e^-(s)$
V		7	$2LiS_1(ads) \rightarrow SEI_1(film) + 2V(ads)$
		8	$SEI_1(film) + 2V(ads) \rightarrow 2LiS_1(ads)$
VI	$LiS_1(ads) \rightleftharpoons LiS_1(e) + V(ads)$	9	$LiS_1(ads) \rightarrow LiS_1(e) + V(ads)$
		10	$LiS_1(e) + V(ads) \rightarrow LiS_1(ads)$
VII	$2LiS_1(e) \rightleftharpoons SEI_1(e)$		
VIII	$S_1(ads) \rightleftharpoons S_1(e) + V(ads)$		
IX	$S_2(ads) \rightleftharpoons S_2(e) + V(ads)$		
X	$S_3(ads) \rightleftharpoons S_3(e) + V(ads)$		
XI	$Li^+(ads) \rightleftharpoons Li^+(e) + V(ads)$		
XII		11	Horizontal surface diffusion: $LiS_1(ads) \rightarrow LiS_1(ads)$
XIII		12	Diagonal surface diffusion: $LiS_1(ads) \rightarrow LiS_1(ads)$

Table 3. Chemical species and their standard state chemical potentials.

Species	μ^0 [kJ] (F^{-1}[V])			method	source
	anode	separator	cathode		
$S_1(ads)$	0 (0)		0 (0)	continuum	chosen
$S_1(e)$		0 (0)		continuum	chosen
$S_2(ads)$	0 (0)		0 (0)	continuum	chosen
$S_2(e)$		0		continuum	chosen
$S_3(ads)$	0 (0)		0 (0)	continuum	chosen
$S_3(e)$		0 (0)		continuum	chosen
$Li(s)$	12.42 (−0.1287)		375.89 (−3.8958)	continuum	fit
$Li^+(ads)$	0 (0)		96.49 (−1)	continuum	chosen
$Li^+(e)$		0		continuum	chosen
$V(s)$	0 (0)		0 (0)	continuum	fit
$V(ads)$	3.86 (−0.04)		3.86 (−0.04)	continuum	chosen
$LiS_1(ads)$	56.93 (−0.59)		56.93 (−0.59)	kMC	chosen
$LiS_1(e)$		55 (−0.57)		continuum	chosen
$SEI_1(film)$	154.38 (−1.6)		154.38 (−1.6)	kMC	fit
$SEI_2(film)$	77.19 (−0.8)		77.19 (−0.8)	kMC	fit
$SEI_3(film)$	57.89 (−0.6)		57.89 (−0.6)	kMC	fit
$SEI_1(e)$		154.38 (−1.6)		continuum	fit

$$a_s = \frac{3\varepsilon_s}{R_s} \tag{5}$$

using the volume fraction of the solid material ε_S and the particle radius R_S. The current density of the electrochemical double layer can be calculated as

$$j_{s,film}^{DL} = j - j_{s,film}^{process} \tag{6}$$

and

$$j_{ads,e}^{DL} = j - j_{ads,e}^{process} \tag{7}$$

for ads/e and s/film interface, respectively. Here j is the current density. Calculation of the species' fluxes through an interface are shown at the example of the flux of species S_1 through the ads/e interface:

$$q_{ads,e}^{S_1} = q_{VII}. \tag{8}$$

Accordingly, the balance for the net flux of S_1 at the adsorption site is applied as

$$q_{ads}^{S_1} = -q_{VII} - q_{II}. \tag{9}$$

Reaction fluxes are determined according to Colclasure et al.,[34] which is shown in the following for the example of reaction I, i.e., an electrochemical reaction, and for the example of reaction VII, i.e., an adsorption process without charge being transferred between the interface, respectively:

$$\frac{o_s}{N_s} q_I = k_I^f \theta^{V(ads)} a^{Li(s)} \exp\left(\frac{\beta \Delta \Phi_{a,film} F}{RT}\right)$$
$$k_I^b \theta^{Li^+(ads)} a^{V(s)} \exp\left(\frac{-(1-\beta)\Delta \Phi_{a,film} F}{RT}\right) \tag{10}$$

and

$$\frac{o_s}{N_s} q_{VII} = k_{VII}^f \theta^{S_1(ads)} \quad k_{VII}^b \theta^{V(ads)} a_{S_1(e)}. \tag{11}$$

Here, o_s is the surface site occupancy number, N_s is the surface site density, θ^m is surface fraction of species m, a^m is the activity of species m, β is the symmetry factor of the reaction, $\Delta\Phi$ is the electrical potential difference at the interface, R is the ideal gas constant, and T is the temperature. The surface fraction of vacancies on the surface is thereby calculated as

$$\theta_{V(ads)} = 1 \quad \theta_{Li^+(ads)} \quad \theta_{S_1(ads)}$$
$$\theta_{S_2(ads)} \quad \theta_{S_3(ads)} \quad \theta_{LiS_1(ads)}. \tag{12}$$

The non ideal activity of lithium and vacancies in the solid material is determined as

$$a^{Li(s)} = x^{Li} \exp \quad \frac{(1 \quad x^{Li})^2}{RT} \sum_{i=0}^{N}\left(A_i^{RK}(2x^{Li} \quad 1)^i \left(1 + \frac{2ix^{Li}}{2x^{Li} \quad 1}\right)\right) \tag{13}$$

and

$$a^{V(s)} = (1 \quad x^{Li}) \exp \quad \frac{(x^{Li})^2}{RT} \sum_{i=0}^{N}\left(A_i^{RK}(2x^{Li} \quad 1)^i \left(1 \quad \frac{2i(1 \quad x^{Li})}{2x^{Li} \quad 1}\right)\right) \tag{14}$$

with A_i^{RK} being Redlich Kister coefficients. The intercalation fraction x^{Li} is determined as

$$x^{Li} = \frac{c^{Li(s)}}{c_{max}}. \tag{15}$$

Activities of species in the electrolyte are calculated assuming ideal solution as

$$a^m = \frac{c^m}{C_m^0}, \tag{16}$$

with C^0 being the standard state concentration.

Forward and backward reaction rate constants are calculated, as shown at the example of reaction I, as Arrhenius expressions

$$k_I^f = A \exp\left(\frac{E_I^A}{RT}\right) \tag{17}$$

and

$$k_I^b = A \exp\left(\frac{(E_I^A \quad \Delta G_I^0)}{RT}\right) \tag{18}$$

with A being the pre-exponential factor, E^A being the activation energy of the forward reaction, and $E^A \quad \Delta G^0$ being the activation energy of the backward reaction. For the sake of simplicity and as we do not consider T dependency A is chosen equally for all processes. Thereby ΔG^0 is the standard state Gibbs free energy of the reaction, which can be determined as

$$\Delta G_I^0 = \mu_{Li(s)}^0 + \mu_{V(ads)}^0 \quad \mu_{V(s)}^0 \quad \mu_{Li^+(ads)}^0 \tag{19}$$

using the standard state chemical potential μ^0 of the involved species. Applied standard state chemical potentials are summarized in Table 3.

To simulate transport processes in the electrolyte within the porous electrode, effective diffusion coefficients are determined as

$$D_{e,eff}^m(x) = \frac{\varepsilon_e(x)}{\tau_e} D_e^m \tag{20}$$

with D_e^m being the bulk diffusion coefficient of species m, ε_e being the electrolyte volume fraction, and τ_e being the tortuosity of the pores filled with electrolyte. Surface films pose an additional resistance for lithium-ion transport, but they also reduce the porosity of the electrode and hinder transport processes in the electrolyte, as shown by.[35] Therefore, the electrolyte volume fraction is calculated as

$$\varepsilon_e(x) = 1 \quad \varepsilon_s \quad a_s r_s d^{film}(x) \tag{21}$$

with d^{film} being the average thickness of the surface film. Thus, increasing the film thickness will reduce the porosity of the electrode and affect transport processes on the electrode scale. Diffusion coefficients are assumed to be constant for solvent and intermediate species and determined as concentration dependent for lithium, as significant concentration gradients for lithium salt during operation can be expected. The concentration dependency is described as a polynomial

$$D_e^{salt} = b_1 + b_2 c_e^{salt} + b_3 c_e^{salt\,2} \tag{22}$$

using the coefficients b_1–b_3. Since no detailed experimental data for concentration dependency of the diffusion coefficient is available for this work, the diffusion coefficient is directly linked to ionic conductivity using Nernst-Einstein relation. We note that this is usually restricted to dilute solutions. Nevertheless, it is applied here to provide a qualitative feasible concentration dependency for ionic conductivity and diffusion coefficient using only experimental data for ionic conductivity as given in section 3.2. The ionic conductivity σ_e is defined as a function of the salt diffusion coefficient:

$$\sigma_e(x) = c_e^{salt}(x) \frac{\mathbf{F}^2 D_e^{salt}(c_e^{salt})}{t_p(2 \quad 2t_p)RT}. \tag{23}$$

According to Legrand et al.,[32] the diffusional ionic transport coefficient is determined as

$$\sigma_{De} = \frac{2RT(t_p \quad \frac{1}{2}))}{\mathbf{F}} \sigma_e. \tag{24}$$

Effective transport coefficients in the solid and electrolyte phase are determined as

$$\sigma_{s,eff} = \varepsilon_s \sigma_s \tag{25}$$

and

$$\sigma_{e,eff}(x) = \frac{\varepsilon_e(x)}{\tau_e} \sigma_e(x), \tag{26}$$

respectively. The difference between electrical potential in the solid and electrolyte phase is determined as

$$\begin{aligned}
\Delta\Phi_{s,e}(x) &= \Phi_s(x) \quad \Phi_e(x) \\
&= \Delta\Phi_{s,film}(x) + \Delta\Phi_{ads,e}(x) + \frac{j(x)R^{film}d^{film}(x)}{a_s r_s}
\end{aligned} \tag{27}$$

and includes the potential drop at the s/film interface, the ads/e interface, and ohmic losses within the surface film, which depends on the current density j, average film thickness d^{film}, and the specific resistance of the film R^{film}.

3.2. Identification of Parameters of Operational Processes

Applied parameters are summarized in Table 5. Most geometrical parameters, i.e., electrode and separator thicknesses, solid volume fraction, and particle sizes, were measured or taken from material data sheets. The main thermodynamic and kinetic parameters were identified as summarized in the following.

First, the thermodynamic parameters of the main intercalation reaction are determined. The Redlich Kister coefficients and the standard state chemical potentials of lithium in the solid $\mu_{Li(s)}^0$ can be identified by measuring equilibrium potential, i.e., OCP, of the electrodes against a lithium reference, as given in Figure 2, and adapting the coefficients to minimize the difference from the calculated equilibrium potential vs Li metal, which is

$$E_{ref}^{eq} = \frac{\mu_{V(s)}^0 + \mu_{Li,metal}^0 \quad \mu_{Li(s)}^0}{\mathbf{F}} + \frac{RT}{\mathbf{F}} \ln\left(\frac{a^{V(s)}}{a^{Li(s)}}\right). \tag{28}$$

The calculated potential is compared to measured values in Figure 2. The identified Redlich Kister coefficients are provided in Table 4 and the identified standard state chemical potentials of lithium in the solid $\mu_{Li(s)}^0$ is provided in Table 3.

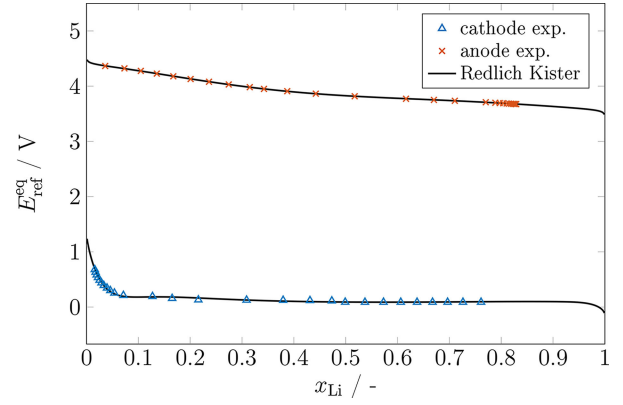Secondly, transport properties of the electrolyte with respect to the main processes can be evaluated by measuring

Figure 2. Measured and calculated equilibrium potential of anode and cathode against a lithium metal reference.

Table 4. Redlich Kister coefficients for anode and cathode.

Coefficient	Anode	Cathode	source
A_1^{RK}	3797	29626	fit
A_2^{RK}	5260	13328	fit
A_3^{RK}	7290	7942	fit
A_4^{RK}	8174	4926	fit
A_5^{RK}	3165	6859	fit
A_6^{RK}	45	0	fit
A_7^{RK}	2079	0	fit
A_8^{RK}	2388	0	fit
A_9^{RK}	1644	0	fit
A_{10}^{RK}	27	0	fit
A_{11}^{RK}	2230	0	fit
A_{12}^{RK}	4818	0	fit
A_{13}^{RK}	7585	0	fit
A_{14}^{RK}	10439	0	fit
A_{15}^{RK}	13277	0	fit
A_{16}^{RK}	16050	0	fit
A_{17}^{RK}	18709	0	fit

electrical conductivity. To achieve a quantitative agreement of electrical conductivity, coefficients b_1–b_3 have been adapted to achieve a good agreement to a data point taken from Plichta et al.[36] and to reproduce the typical non-monotonous concentration dependency of lithium-ion battery electrolytes, as provided in.[37] The applied concentration dependency is shown in Figure 3. This yields a good quantitative description of the electrolyte conductivity, which is the main feature of the electrolyte. However, future work should refine parameter identification of the electrolyte and include measurement of the concentration dependency of diffusion coefficient and transference number in concentrated solutions.

Finally, the main kinetic parameters, i.e., activation energies, $E_1^{A,a}$ and $E_1^{A,c}$, solid diffusion coefficients, $D_s^{Li,a}$ and $D_s^{Li,c}$, and electrical conductivity within the solid, σ_s^a and σ_s^c, as well as unknown geometrical properties such as tortuosity, τ_e^a and τ_e^c, are identified using C-rate test data as shown in Figure 4. It should be noted that the parameter identification, as shown here, does not provide proof for the uniqueness of the

Table 5. Battery parameters.

Parameter	Anode	Separator	Cathode	Source
double layer capacitance $C_{s,film}^{DL}$ [F m^{-2}]	0.1		0.2	chosen
double layer capacitance $C_{ads,e}^{DL}$ [F m^{-2}]	0.1		0.2	chosen
maximal concentration in solid c_{max} [mol m^{-3}]	32000		30000	chosen
roughness factor r_s [ ]	10		1	chosen
thickness δ [m]	55.25 × 10^{-6}	20 × 10^{-6}	60 × 10^{-6}	measured
solid diffusion coefficient D_s^{Li} [m^2 s^{-1}]	1.17 × 10^{-13}		7.3294 × 10^{-16}	fit
diffusion coefficient of S$_1$ $D_e^{S_1}$ [m^2 s^{-1}]		1 × 10^{-13}		chosen
diffusion coefficient of S$_2$ $D_e^{S_2}$ [m^2 s^{-1}]		1 × 10^{-12}		chosen
diffusion coefficient of S$_3$ $D_e^{S_3}$ [m^2 s^{-1}]		1 × 10^{-14}		chosen
diffusion coefficient of LiS$_1$ $D_e^{LiS_1}$ [m^2 s^{-1}]		0		chosen
coefficients for salt diffusion (b_1,b_2,b_3) [mol,m,s]		(2.5 × 10^{-10}, 1.63 × 10^{-13}, 3.183 × 10^{-17})		fit
surface diffusion of LiS$_1$ $D_{ads}^{LiS_1}$ [m^2 s^{-1}]	1 × 10^{-14}		1 × 10^{-14}	chosen
transference number t_p [ ]		0.3		chosen
tortuosity τ_e [ ]	13.8918	3.03	2.3041	fit
solid volume fraction ε_s [ ]	0.65	0.5	0.6	measured
solid electrical conductivity σ_s [S m^{-1}]	672.416		5.4179	fit
electrical resistance surface film R^{film} [Ω m]		4 × 10^6		chosen
particle radius R_s [m]	5.5 × 10^{-6}		11.5 × 10^{-6}	material info.
temperature T [K]		300		chosen
site density N_s [m^{-2}]		2.77778 × 10^{18}		chosen
site occupancy number o_s [mol^{-1}]		6.022 × 10^{23}		chosen
grid size ΔL [m]		6 × 10^{-10}		chosen
standard state concentration Li$^+$(e) $C_{Li^+(e)}^0$ [mol m^{-3}]		1000		chosen
standard state concentration LiS$_1$(e) $C_{LiS_1(e)}^0$ [mol m^{-3}]		1000		chosen
standard state concentration SEI$_1$(e) $C_{SEI_1(e)}^0$ [mol m^{-3}]		1000		chosen
standard state concentration S$_x$ $C_{S_x(e)}^0$ [mol m^{-3}]		4000		chosen
pre exponential factor A [s^{-1}]	1 × 10^{10}		1 × 10^{10}	chosen
activation energy E_I^A [kJ] (F^{-1}[V])	2.89 (0.03)		132474.36 (−1.373)	fit
activation energy E_{II}^A [kJ] (F^{-1}[V])	18.33 (0.19)		18.33 (0.19)	chosen
activation energy E_{III}^A [kJ] (F^{-1}[V])	19.3 (0.20)		19.3 (0.20)	chosen
activation energy E_{IV}^A [kJ] (F^{-1}[V])	20.26 (0.21)		20.26 (0.21)	chosen
activation energy E_V^A [kJ] (F^{-1}[V])	1.93 (0.02)		1.93 (0.02)	chosen
activation energy E_{VI}^A [kJ] (F^{-1}[V])	0.96 (0.01)	0.96 (0.01)	0.96 (0.01)	chosen
activation energy E_{VII}^A [kJ] (F^{-1}[V])	33.77 (0.35)		33.77 (0.35)	chosen
activation energy E_{VIII}^A [kJ] (F^{-1}[V])	28.95 (0.3)		28.95 (0.3)	chosen
activation energy E_{XI}^A [kJ] (F^{-1}[V])	28.95 (0.3)		28.95 (0.3)	chosen
activation energy E_X^A [kJ] (F^{-1}[V])	28.95 (0.3)		28.95 (0.3)	chosen
activation energy E_{XI}^A [kJ] (F^{-1}[V])	28.95 (0.3)		28.95 (0.3)	chosen
specific activation energy $\hat{E}_{film}^A$ [kJ m^{-1}] (F^{-1}[V m^{-1}])	8.29 × 10^8 (8.6 × 10^6)		8.29 × 10^8 (8.6 × 10^6)	fit
bonding energy E_{bond}^A(LiS$_1$|SEI$_1$) [kJ] (F^{-1}[V])	7 (0.0725)		7 (0.0725)	chosen
bonding energy E_{bond}^A(LiS$_1$|SEI$_2$) [kJ] (F^{-1}[V])	3 (0.0311)		3 (0.0311)	chosen
bonding energy E_{bond}^A(LiS$_1$|SEI$_3$) [kJ] (F^{-1}[V])	3 (0.0311)		3 (0.0311)	chosen
bonding energy E_{bond}^A(LiS$_1$|solid) [kJ] (F^{-1}[V])	7 (0.0725)		7 (0.0725)	chosen
bonding energy E_{bond}^A(SEI$_1$|SEI$_1$) [kJ] (F^{-1}[V])	12 (0.1244)		12 (0.1244)	chosen
bonding energy E_{bond}^A(SEI$_2$|SEI$_3$) [kJ] (F^{-1}[V])	4 (−0.0415)		4 (−0.0415)	chosen

identified parameter set. Moreover, as activation energies have been parameterized only for one temperature, they only provide a feasible reaction rate for this temperature but do not accurately describe actual temperature dependency. However, good agreement between simulated and measured electrical potential is achieved.

In the case of the multiscale simulation, the continuum model relies on kMC input parameters, i.e., $\theta_{LiS_1(ads)}$, q_{II}, q_{III}, q_{IV}, q_{VI}, and d^{film}, which is shown in Figure 1. The reaction rate fluxes q need to be considered if the contribution of side reactions is significant. This is the case during the first charge/discharge cycles of the battery. However, single discharge cycles after

formation are assumed to have negligible progress in degradation, i.e., the degradation state is set to quasi static state. The assumption has been applied to identify the parameters of the operational processes, i.e., normal charge/discharge behavior of the battery. In detail, for parameter identification shown in this section, we assumed $\theta_{LiS_1(ads)} = 0$, $q_{II} = 0$, $q_{III} = 0$, $q_{IV} = 0$, $q_{VI} = 0$, and $d^{film} = 4 × 10^{-8}$ m, i.e., corresponding to no side reactions and an assumed film thickness of 40 nm. For the purpose of this work, the initial guess was sufficiently precise. However, in future work film thickness can be adapted after simulation of formation in an iterative process, which would refine the parameter identification procedure. Identifying
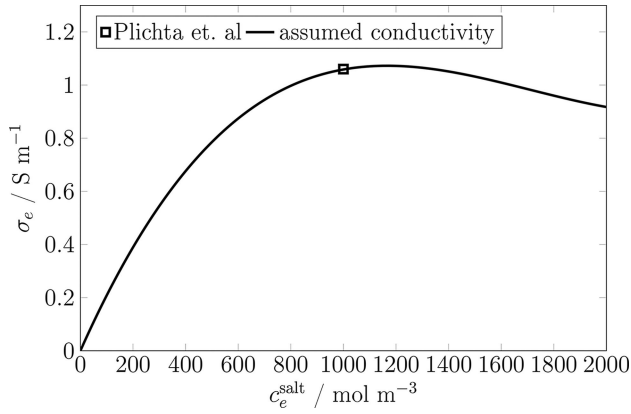
Figure 3. Electrolyte conductivity as a function of salt concentration and measurment point taken from Pilcha et al.[36]
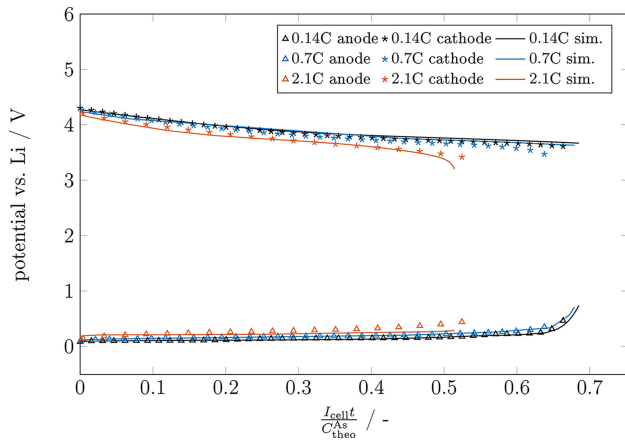

Figure 4. Measurement and simulation of a C rate test for anode and cathode potential versus lithium reference placed in the center of the separator.

parameters of the operational processes a priori to the analysis of the first charge cycle, allows the separation of the contribution of the operational processes during the first charge cycle and thus enables the parameter identification for the side reactions.

4. Microscopic Scale

4.1. Kinetic Monte Carlo Model

In order to model the detailed microscopic processes at the film surface and the heterogeneous film growth, the continuum model, as shown in the previous section, is directly coupled with a kMC model. In this article, no details are given about the numerical coupling of both codes. However, details can be found in our previous work.[28,29]

In every time step i of the kMC model, the kMC algorithm performs the following actions:

1. calculate microscopic rate, $\Gamma_i^{l,j}$ for every possible microscopic process $j \in \{z \mid z \in \mathbb{N}, z \leq n^j\}$ on every lattice site $l \in \{z \mid z \in \mathbb{N}, z \leq n^l\}$.
2. calculate time step, Δt.
3. select one process $J_i \in \{z \mid z \in \mathbb{N}, z \leq n^j\}$ and lattice site $L_i \in \{z \mid z \in \mathbb{N}, z \leq n^l\}$ according to microscopic rates $\Gamma_i^{l,j}$ (details below).
4. perform process J_i.
5. if end time of simulation not reached go to 1.

The model is set up as a solid-on-solid, i.e., $2+1$D, model. The model structure is illustrated in Figure 1 (C). The state of the film sites f in a 3D cubic system is defined as

$$\vartheta_i^{\text{film}}(f) \in \{\text{solid}, \text{SEI}_1, \text{SEI}_2, \text{SEI}_3, \vartheta_i^{\text{lattice}}\}. \tag{29}$$

The bottom row of the 3D film is defined to be filled with solid, e.g., anode or cathode active material; the other sites can be either a SEI component, or a lattice site, where species are adsorbed. Film growth is restricted to vertical growth with respect to the solidsurface. The lattice site is defined as being on top of the highest solid component, as illustrated in Figure 1 (C). Microscopic processes on the surface are considered to be on a 2D lattice, with lattice site l. Neighbors of a given film site f are indicated as f'. Horizontal neighbors of a lattice site l are indicated as l' and diagonal neighbors are indicated as l''. A film site corresponding to a lattice site l is indicated as $f(l*)$, and film site directly below a lattice site are indicated as $f(l)$. There are two lattice site states

$$\vartheta_i^{\text{lattice}}(l) \in \{\neg\text{LiS}_1, \text{LiS}_1\} \tag{30}$$

where LiS_1 corresponds to a surface site covered with a LiS_1 species, and $\neg\text{LiS}_1$ corresponds to a surface not covered with a LiS_1 species, i.e., possibly covered with other species or being vacant. The probability that a $\neg\text{LiS}_1$ site is covered with a species m is determined as

$$\theta_{\neg\text{LiS}_1}^m = \frac{\theta^m}{1 - \theta^{\text{LiS}_1}}. \tag{31}$$

The direct inclusion of only a few species in the kMC model, with other species being covered by the continuum model, enables a long simulation time length for multiscale simulation and has been shown in detail in [28].

In every kMC step i, the microscopic rate $\Gamma_i^{l,j}$ of every considered microscopic process j and every lattice site l is calculated. Considered microscopic processes j are given in Table 2. The table also shows the corresponding macroscopic processes. In Table 6 assumed requirements, i.e., for solids and species on neighboring sites, the performed action in case of selection, and equations for calculation of the microscopic rates are given.

Within the kMC algorithm the time step length is calculated based on a uniformly distributed random number $\zeta_1 \in (0, 1)$ as

Table 6. Microscopic processes j within the kMC model, according to Table 2 and the corresponding lattice and film site states before and after the process.

Microscopic j	state at i	state at $i+1$	microscopic rate $\Gamma_i^{l,j}$
1	$\vartheta_i^{lattice}(l) = \neg LiS_1$ $\vartheta_i^{lattice}(l') = \neg LiS_1$	$\vartheta_{i+1}^{lattice}(l) = LiS_1$	$k_{II}^f[\theta_{\neg LiS_1}^{Li^+}][\theta_{\neg LiS_1}^{S_1}]p_{cat}$
2	$\vartheta_i^{lattice}(l) = LiS_1$ $\vartheta_i^{lattice}(l') = \neg LiS_1$	$\vartheta_{i+1}^{lattice}(l) = \neg LiS_1$	$k_{II}^b[\theta_{\neg LiS_1}^V]p_{an}p_{bond,f(l^*)}$
3	$\vartheta_i^{lattice}(l) = \neg LiS_1$ $\vartheta_i^{lattice}(l') = \neg LiS_1$	$\vartheta_{i+1}^{film}(f(l^*)) = SEI_2$	$k_{III}^f[\theta_{\neg LiS_1}^{text Li^+}][\theta_{\neg LiS_1}^{S_2}]p_{cat}$
4	$\vartheta_i^{lattice}(l) = \neg LiS_1$ $\vartheta_i^{lattice}(l') = \neg LiS_1$	$\vartheta_{i+1}^{film}(f(l)) = \vartheta_{i+1}^{lattice}(l)$	$k_{xtIII}^b[\theta_{\neg LiS_1}^V]^2 p_{an}p_{bond,f(l)}$
5	$\vartheta_i^{lattice}(l) = \neg LiS_1$ $\vartheta_i^{lattice}(l') = \neg LiS_1$	$\vartheta_{i+1}^{film}(f(l^*)) = SEI_3$	$k_{IV}^f[\theta_{\neg LiS_1}^{ext Li^+}][\theta_{\neg LiS_1}^{S_3}]p_{cat}$
6	$\vartheta_i^{lattice}(l) = \neg LiS_1$ $\vartheta_i^{lattice}(l') = \neg LiS_1$	$\vartheta_{i+1}^{film}(f(l)) = \vartheta_{i+1}^{lattice}(l)$	$k_{xtIV}^b[\theta_{\neg LiS_1}^V]^2 p_{an}p_{bond,f(l)}$
7	$\vartheta_i^{lattice}(l) = LiS_1$ $\vartheta_i^{lattice}(l') = LiS_1$	$\vartheta_{i+1}^{lattice}(l) = \neg LiS_1$ $\vartheta_{i+1}^{lattice}(l') = \neg LiS_1$ $\vartheta_{i+1}^{film}(f(l^*)) = SEI_1$ $\vartheta_{i+1}^{film}(f(l'^*)) = SEI_1$	k_V^f
8	$\vartheta_i^{lattice}(l) = \neg LiS_1$ $\vartheta_i^{lattice}(l') = \neg LiS_1$ $\vartheta_i^{film}(f(l)) = SEI_1$ $\vartheta_i^{film}(f(l')) = SEI_1$	$\vartheta_{i+1}^{lattice}(l) = LiS_1$ $\vartheta_{i+1}^{lattice}(l') = LiS_1$ $\vartheta_{i+1}^{film}(f(l)) = \vartheta_{i+1}^{lattice}(l)$ $\vartheta_{i+1}^{film}(f(l')) = \vartheta_{i+1}^{extlattice}(l')$	$k_V^b[\theta_{\neg LiS_1}^V]^2 p_{bond,f(l)}p_{bond,f(l')}$
9	$\vartheta_i^{lattice}(l) = LiS_1$	$\vartheta_{i+1}^{lattice}(l) = \neg LiS_1$	$k_{VI}^f p_{bond,f(l^*)}$
10	$\vartheta_i^{lattice}(l) = \neg LiS_1$	$\vartheta_{i+1}^{lattice}(l) = LiS_1$	$k_{VI}^b[\theta_{\neg LiS_1}^V][a_{LiS_1(e)}]$
11	$\vartheta_i^{lattice}(l) = LiS_1$ $\vartheta_i^{lattice}(l') = \neg LiS_1$	$\vartheta_{i+1}^{lattice}(l) = \neg LiS_1$ $\vartheta_{i+1}^{lattice}(l') = LiS_1$	$\frac{D_{asd}^{LiS_1}}{2\Delta L^2}p_{bond,f(l^*)}$
12	$\vartheta_i^{lattice}(l) = LiS_1$ $\vartheta_i^{lattice}(l'') = \neg LiS_1$	$\vartheta_{i+1}^{lattice}(l) = \neg LiS_1$ $\vartheta_{i+1}^{lattice}(l'') = LiS_1$	$\frac{D_{asd}^{LiS_1}}{4\Delta L^2}p_{bond,f(l^*)}$

$$\Delta t_{i+1}^{kMC} = \frac{\ln(\zeta_1)}{\Gamma_i^{tot}}, \tag{32}$$

thus the time at the following time step $i+1$ can be calculated with

$$t_{i+1}^{kMC} = t_i^{kMC} + \Delta t_{i+1}^{kMC}. \tag{33}$$

Further, in every kMC step, one of the possible microscopic processes is selected using a second uniformly distributed random number $\zeta_2 \in (0, 1)$ according to

$$\frac{\sum_{k=1}^{L_i}\sum_{j=1}^{J_i-1}\Gamma_i^{k,j}}{\Gamma_i^{tot}} < \zeta_2 \leq \frac{\sum_{k=1}^{L_i}\sum_{j=1}^{J_i}\Gamma_i^{k,j}}{\Gamma_i^{tot}} \tag{34}$$

with J_i being the selected process and L_i being the selected lattice site. The total microscopic rate Γ_i^{tot} is calculated as

$$\Gamma_i^{tot} = \sum_{k=1}^{n^k}\sum_{j=1}^{n^j}\Gamma_i^{k,j}. \tag{35}$$

A boolean, which indicates the selection of a process j within a kMC step i can be determined as

$$\Psi_i^j = \begin{cases} 1, & \text{if } J_i = j \\ 0, & \text{otherwise} \end{cases}. \tag{36}$$

The single processes and equations for calculating the corresponding microscopic rates $\Gamma_i^{l,j}$ are given in Table 6. These rates can depend on thickness of the film and breakage of bonds to nearest neighbors, as explained in the following.

Several growth limiting steps are assumed in literature, e.g., electron tunneling, electron conduction, solvent diffusion or lithium-interstitial diffusion, which have been studied using continuum models for aging during battery storage[23] or formation.[24] Possibly there is a competition of several transport mechanisms in parallel[38] and a two layer structure with a dense inner and porous outer layer.[39] Siqi et al. identified detailed lithium and electron transport properties within Li_2CO_3 using DFT simulations, which also indicates that the transport mechanism depend on various factors, such as molecular structure, potential, and active material. Tang et al.[24] provided a detailed study to identify growth limiting steps during formation, but also conclude that the transport mechanism can depend on the electrode structure and may differ between formation and capacity fade.

In this work, the probability of an electron leaking through the surface film is assumed to exponentially decrease with film thickness. This is usually associated to electron tunneling, and

has been applied frequently, e.g.[20,22] This assumption provides good agreement to experiments shown in this work. We note that as outlined above, the actual mechanism strongly depends on the SEI composition and structure. Further, we do not consider limitation of film growth originating from film porosity, but only consider the impact of reduced porosity on electrode scale according to Sikha et al.[35] due to equation 21. Identification of mechanisms of growth limitation are not within the scope of this article and thus, actual mechanisms may differ and can be significantly more complex.

The following equations for cathodic and anodic reactions are assumed, respectively:

$$p_{\text{cat},l} = \exp\left(-\frac{(1-\beta)\Delta\Phi F - \hat{d}^{\text{film}}(l)\,\hat{E}^A_{\text{film}}}{RT}\right) \tag{37}$$

and

$$p_{\text{an},l} = \exp\left(\frac{\beta\Delta\Phi F - \hat{d}^{\text{film}}(l)\,\hat{E}^A_{\text{film}}}{RT}\right). \tag{38}$$

Therein, $\hat{d}^{\text{film}}(l)$ is the film thickness at the lattice site l. Further, the probability of a bond breakage between two neighboring sites f and f' is calculated according to [40] as

$$p_{\text{bond},f} = \exp\left(\frac{\sum_{f'} E^A_{\text{bond}}(\vartheta^{\text{film}}(f)|\vartheta^{\text{film}}(f'))}{RT}\right). \tag{39}$$

The output of the kMC model, i.e., input parameters to the continuum model, is provided in the following equations. The average thickness of the surface film is determined as

$$d^{\text{film}} = \frac{\sum_l \hat{d}^{\text{film}}}{n^l} \tag{40}$$

and the reaction fluxes q are determined as shown at the example of reaction II as

$$q_{\text{II}} = \frac{\sum_{\text{seq}} \Psi_i^{j-1} - \sum_{\text{seq}} \Psi_i^{j-2}}{\Delta t_{\text{seq}} n^l \Delta L^2 N_s}. \tag{41}$$

Further, the average surface fraction of species LiS_1 is determined. Output data are evaluated within a sequence (seq). Details about sequences and model coupling can be found in [28]. Within the multiscale simulations, information is sequentially exchanged between the kMC and the continuum model. Exchanged data are summarized in Figure 1.

4.2. Identification of Parameters of Degradation Process

The applied experiments are not particularly designed to identify parameters of complex surface film growth mechanisms, but are rather standard characterization experiments. Further, presently neither adequate experimental nor theoretical data are available to describe decomposition reactions for an electrolyte with this complexity. Therefore, instead, we

construct a lumped degradation mechanism, which (i) includes comprehensive heterogeneity, but at the same time is (ii) simple enough to generate illustrative results with traceable multiscale effects, and (iii) enables one to identify parameters that achieve quantitative agreement with the experimental data. The presented results do not claim to provide details about degradation chemistry, but instead demonstrate the simulation method and provide evidence for multiscale effects. In the following, the constructed mechanism, motivation for the assumptions are outlined.

As given in Section 2.1, experiments were carried out using a tertiary electrolyte with three solvents, i.e., EC, DMC, and EMC. Components are electrochemically unstable in the applied potential window and thus at least three different SEI components can be expected. Thus, for the presented analysis, a tertiary electrolyte with solvents S_1, S_2 and S_3 is assumed.

Rate constants and decomposition potentials vary for different solvents.[41] Potentials for decomposition are reported to be between 0.6–1 V.[1,42] Xu et al.[43] indicate that solvents have different lowest unoccupied molecule orbitals, which have a high impact on reaction ability and thus reduction potential. For instance, they showed that the value of EC is much lower than the one of EMC, which denotes that theoretically EC decomposes at higher potentials than EMC. In the presented experimental data for the first charge cycle, as given in Figure 5,
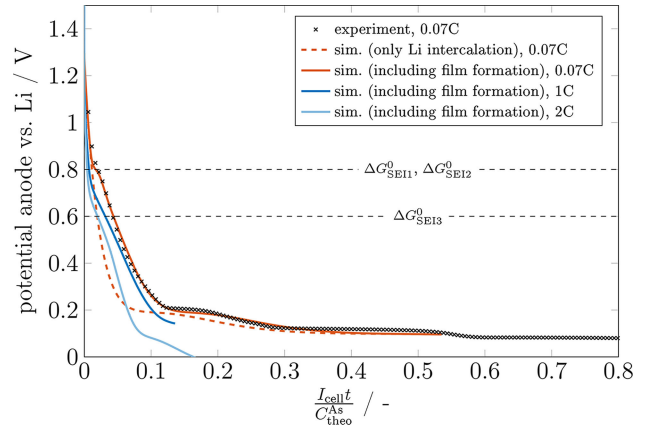

Figure 5. Potential during first charge, i.e., film formation, of battery with 0.07 C for experiment and 0.07 C, 1 C, and 2 C for the simulation.

the decomposition reaction starts at 0.8 V. Thus, the decomposition potential of SEI_1 and SEI_2 is chosen with 0.8 V. To investigate the effect of the outlined variation in decomposition potential for different solvents, a potential of 0.6 V is chosen in case of SEI_3.

Agabura et al.[5] suggested various mechanisms for solvent decomposition. For instance, they suggested that EMC may decompose in a two electron process with two lithium ions to form lithium carbonate. An et al.[1] suggested that EC possibly first reacts with e− and Li+, and in a second step further decomposes to form for instance lithium ethylene dicarbonate. As mechanisms are still under discussion and often several

possible pathways are suggested, here the following lumped mechanisms are assumed:

$$S_1 + e^- + Li^+ \rightleftharpoons LiS_1 \qquad (42)$$

$$2\,LiS_1 \rightleftharpoons SEI_1 \qquad (43)$$

$$S_2 + e^- + Li^+ \rightleftharpoons SEI_2 \qquad (44)$$

and

$$S_3 + e^- + Li^+ \rightleftharpoons SEI_3 \qquad (45)$$

As a standard case the most simple possible decomposition mechanism is chosen, where a solvent reacts with Li^+ and e to form a SEI component. This mechanism is chosen for decomposition of S_2 and S_3. For S_1 a slightly more complex mechanism is chosen, where first an intermediate, LiS_1, is formed by reaction of S_1 with a Li^+ and an e . LiS_1 diffuses on the surface and reacts with neighboring species on the surface to form the SEI_1. With this, the decomposition of S_1 includes two reaction steps. The second step, i.e., Equation 43, does not involve an electron transfer and thus can also take place within the electrolyte solution after LiS_1 desorption.

Since the mechanism does not include any electrode specific components, consistency requires consideration for both electrodes, i.e., anode and cathode. However, due to the high potential no film formation takes place at the cathode.

As outlined previously, the SEI is often found to have a heterogeneous structure, which can be caused by crystalline growth[8] or formation of clusters.[9] In this work, we introduce according heterogeneity as explained in the following. We assume that the intermediate LiS_1 has stronger binding energies to its decomposition product SEI_1. Further, we assume that the chemical energy of the SEI_1 decreases with increasing number of bonds. This denotes that large clusters are favorable. Finally, we assume that SEI_2 and SEI_3 have repulsive bonds, which denotes the chemical energy is increased, i.e., activation energy for reaction is decreased, if they are on neighboring sites.

In Figure 5, the measured potential during the first charge of the battery is presented. Further, the simulation results for this charge process using the continuum model, i.e., only Li intercalation, is shown as dashed red line. It can be seen that there is a significant deviation between measurement and simulation. Since the model is in good agreement with the experiments after film formation, this deviation can be assigned to the side reactions, i.e., film formation. It can be seen that at a certain potential, i.e., approximately 0.8 V, there is a small potential plateau. Further, the potential at the beginning of charge is significantly higher. The deviation corresponds to the electric charge, which is consumed by the side reactions in addition to the operational process of lithium intercalation.

The height of the observed plateau corresponds to the Gibbs free energy between educts and products of the single SEI reaction and thus triggers the respective reactions at potentials below the corresponding potential. The potential has been set by choosing respective values for the standard state

chemical potential μ^0 of the SEI components in the surface film. The length of the plateau mainly corresponds to the time which is needed to form a stable initial film, i.e., the first depletion or desorption of solid SEI components, after which rates of side reactions are reduced according to Equations 37 and 38. The slope at the beginning of the first discharge mainly corresponds to the specific activation energy for electron leakage $\hat{E}^A$. Based on these findings, parameters $\mu^0_{SEI_1(ads)}$, $\mu^0_{SEI_2(ads)}$, and $\hat{E}^A$ have been selected to achieve agreement between multiscale simulation and experiment for the first charge of the battery with 0.07 C, which is shown in Figure 5.

In Figure 5, further, potential is shown for higher C-rates, i.e., 0.5 C, 1 C, and 2 C. Goers et al.[42] presented experimental results for formation with variation of the applied current. Their experiments are qualitatively in agreement with the presented simulation results for electrode potential during the first charge. They observed, that the formation plateau "remained almost constant with varying overall current density" and it "shifted with increasing current density towards more negative potentials".

Note that the chosen decomposition mechanisms, i.e., Equation 42–45, are lumped and most of the parameters of the underlying microscopic processes remain unknown. Thus, the results will not provide details about the actual mechanism within the analyzed cell. Future work will be needed to refine the parameterization and allow more detailed kinetic studies. However, the choice of these mechanisms and parameters fulfill the conditions i-iii as stated at the beginning of this section. Key parameters corresponding to the formation process have been selected to achieve good agreement between the measured and simulated potential during film formation, which denotes that the quantity of the side reaction is validated. Therefore simulation results shown here are valid for an analysis of general aspects of interaction between main intercalation, side reactions, and heterogeneous film growth, which is the scope of this paper and discussed in the following section.

5. Results and Discussion

In the previous sections, the model and a general procedure to adjust parameters to fit experimental data has been outlined. In this section, a parameterized model is used to provide evidence for multiscale effects, which with a high likelihood occur in a similar manner in real lithium-ion batteries. Simulations are quantitatively in very good agreement with the presented experiments. This denotes that the magnitude of SEI components produced, as well as the potentials of the decomposition reactions, are plausible. On this basis, no conclusions about the actual cell chemistry and film structure can be made, but instead the general aspects of the multiscale interaction and their potential impact on film structure can be revealed to illustrate the current dependence of multiscale effects.

Additionally to the experimentally applied formation procedure, i.e., 0.07 C, 2.15 A m ^{2}, simulations are performed with 1 C, 30.7 A m ^{2}, and 2 C, 61.4 A m ^{2}, which are considerably faster procedures. In the following, first, the major observations

of the simulations are outlined, and afterwards the multiscale interaction is discussed.

5.1. Simulation Results

In Figure 6 (A) average thickness, out of 9 simulated kMC instances, of surface film for formation with 0.07 C at three
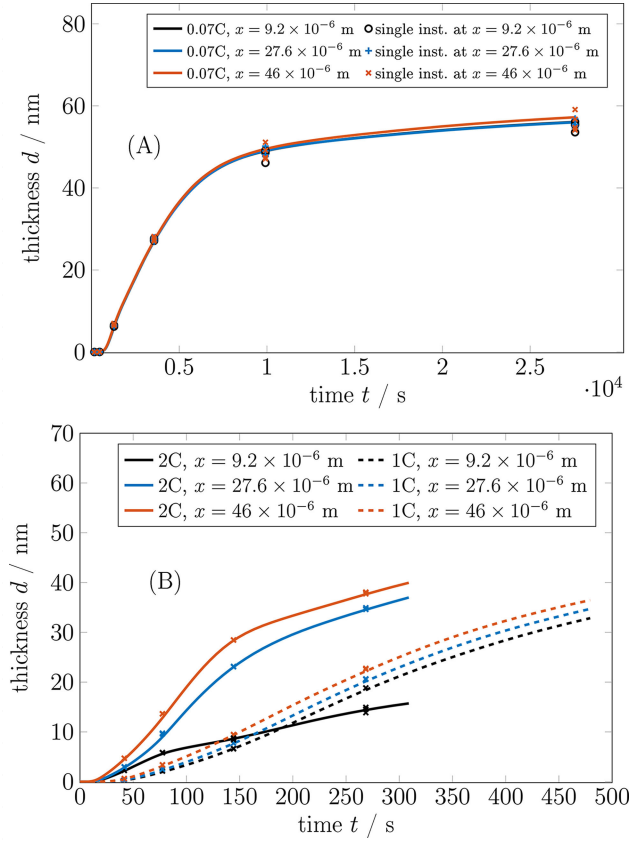

Figure 6. Film thickness at three positions x in the anode for simulation of formation with (A) 0.07 C and (B) 1 C and 2 C. Further the result for single kMC instances at characteristic time points are given to elucidate statistical fluctuations.

different positions x within the electrode is shown, while small values of x corresponding to positions close to the current collector. It can be seen, that film thickness monotonously increases with time. Film growth rate decreases at about 1×10^4 s. This strongly correlates to the potential change at this time shown in Figure 5. We note that this correlation is mainly related to the defined electron leakage mechanism given with Equation 37–38. This is usually associated with electron tunneling, which should be limited to a few nanometers. With significantly greater thicknesses than 5 nm the leakage mechanism may change, which could yield a deviating slope. Further, it can be seen that there is a small difference in film thickness along the x coordinate with higher film thickness close to the separator. Further, the values for film thickness of four single instances of the kMC model are given. It can be seen that there is a significant fluctuation in thickness of up to approximately 3 nm, which is increasing with time t and which is considerably larger than the differences along electrode position x.

In Figure 7 (A–C), the corresponding molecular structure of the surface film after film formation is shown at the same three positions within the electrode for the four parallel kMC instances. It can be seen that the assumed decomposition mechanisms indeed yield significant heterogeneity in film structures. Moreover, it can be seen that the four parallel instances deviate due to the stochastic nature of the kMC model. There is a significant stochastic fluctuation at all three positions in the electrode, therefore no quantitative deviations of composition along x axis is given for this low C-rate. Structures show a SEI_1 and SEI_2 rich region close to the electrode surface and region with all three components closer to the electrolyte. In particular close to the solid and close to the electrolyte, larger clusters of the SEI_1 component can be found. The formation of clusters can be assigned to the assumption of strong surface binding of LiS_1 to SEI_1, as well as strong binding energies between neighboring SEI_1 components. Small clusters, i.e., approximately 10 molecules, of SEI_2 and SEI_3 components can be observed, as they are not randomly distributed, which is assigned to the repulsive force assumed between those components.

In Figure 8, the composition of the surface film as a function of the film height is shown in detail. The fraction of the three components is shown for the instance to the left of Figure 7 (A–C). Further, the maximum and minimum fraction of SEI_1, out
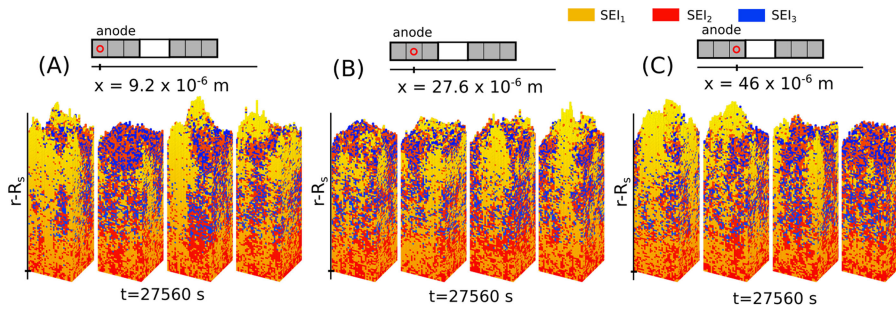

Figure 7. Film composition of one kMC instance after formation with 0.07 C at $t = 27560$ s. Maximum and minimum values of SEI_1 fraction out of four kMC instances are indicated. Further, electrode potential at electrode (s), left and right of film, and electrolyte (e) is shown.
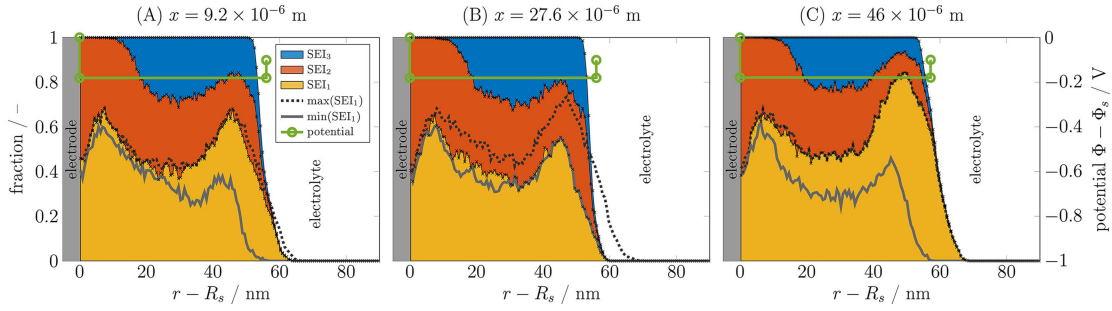
Figure 8. Composition and film structure of a kMC instance at $t = 269$ s during the first charge with 1 C at position $x = 9.2 \times 10^{-6}$ m (A), $x = 27.6 \times 10^{-6}$ m (B), and $x = 46 \times 10^{-6}$ m (C). For SEI$_1$ composition, also the maximum and minimum value out of four instances is shown. Further, electrode potential at electrode (s), left and right of film, and electrolyte (e) is shown.

of the four instances shown in Figure 7, is indicated to illustrate the effect of stochasticity. It can be seen that SEI$_3$ appears only after a certain height, $r - R_S > 10$ nm. This observation can be assigned to the Gibbs free energy of the SEI$_3$ decomposition, which is at lower potentials, i.e., 0.6 V, as shown in Figure 5. Further, there is a peak for the fraction of SEI$_1$ at low heights, $r - R_S = 8$ nm and higher heights, $r - R_S = 50$ nm. In Figure 7 it can be seen that those peaks correspond to large clusters of SEI$_1$. Finally, by indicating the minimum and maximum values for SEI$_1$ fraction, the statistical fluctuation, as observed previously, is quantified. It can be seen that fluctuation is rather high and increases with increasing film thickness. However, the two peaks in SEI$_1$ fraction are statistically relevant and can be found for all four instances at all positions.

Results in Figure 7 and 8 show that the chosen heterogeneity and parameter assumptions yield a distinct structure of the surface film.

In Figure 5, the anode potential against a lithium metal reference is shown for simulation of formation with 1 C and 2 C, respectively. It can be seen that potentials of the anode are shifted towards lower potentials with increasing C-rates due to significant kinetic potential losses. Further, results show a slight SEI formation plateau for both simulations. The potential shifts to more negative potentials, as can be also seen in Figure 5.

In Figure 6 (B), the average film thickness at the anode for formation with 1 C and 2 C is shown at the three positions. It can be seen that for all simulations, film thickness is continu-

ously increasing at all positions. In general, film thickness is highest close to the separator, i.e., at position $x = 46 \times 10^{-6}$ m. For simulation of formation with 2 C. The film thickness close to the separator is more than twice as high as film thickness close to the current collector. The difference in film thickness considerably increases with increasing C-rates. In simulation results shown here, film growth rate increases with increasing C-rate. For formation with 2 C, the slope of the film thickness considerably differs by approximately 10 % for different positions. In contrast, at formation with 1 C, the slope of film thickness is comparable at all investigated positions. Further, thickness of four single instances of the kMC is shown. It can be seen that there is no significant difference between the instances and the average value. Only for 2 C and small values for x, a slight fluctuation of thickness can be observed. Results suggest that with higher formation currents, macroscopic differences in film thickness along electrode position may be observed. Differences in local conditions, such as species concentrations and potentials, affect atomistic processes and structuring of the film, which is discussed below. In the following, composition and film structure along the electrode position are discussed in detail.

In Figure 9 (A–C), surface film composition along film thickness at the three electrode coordinates x are shown for 1 C at 269 s. This time is still during the active buildup of SEI, as seen in Figure 6, but it enables direct comparison with 2 C formation, where 269 s is at the end of formation. It is
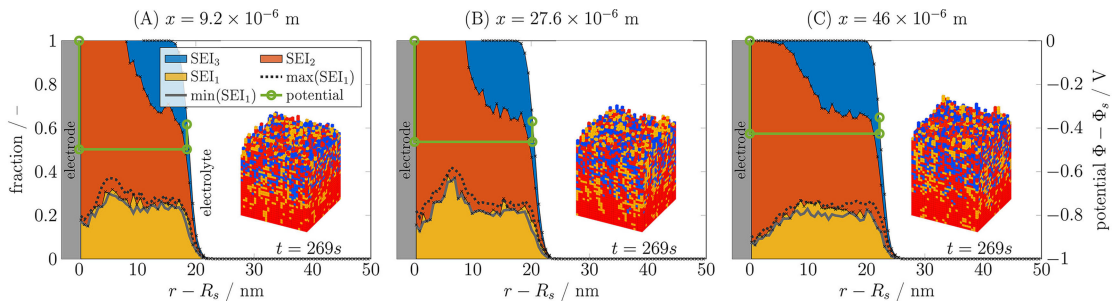

Figure 9. Composition and film structure of a kMC instance at $t = 269$ s during the first charge with 2 C at position $x = 9.2 \times 10^{-6}$ m (A), $x = 27.6 \times 10^{-6}$ m (B), and $x = 46 \times 10^{-6}$ m (C). For SEI$_1$ composition, also the maximum and minimum value out of four instances is shown. Further, electrode potential at electrode (s), left and right of film, and electrolyte (e) is shown.

furthermore ca. 100x shorter than the time of the structures illustrated for 0.07 C. In any case, the structures in the film remain constant with time, as modifications just occur at the surface, enabling a sound comparison at all times. First, the difference between film composition and structure between formation with 1 C and 0.07 C, shown in Figure 7 and 8, is discussed. As can be seen, the fraction of SEI_1 is significantly larger at lower charging rates. Further, a distinct peak of SEI_1 fraction at 10 and 45 nm, as seen with low C-rates, can not be seen at 1 C formation, but only a slight peak at 8 nm can be seen. Moreover, the clusters of SEI_1 are much smaller at higher charging rates. No significant difference in composition and structure can be seen between 0 and 10 nm. At thicknesses higher than 10 nm, an increasing content of SEI_3 can be seen. This second part is slightly thicker close to the separator. As can be seen, the statistical fluctuation of SEI_1 component is significantly reduced at 1 C compared to 0.07 C, which denotes less local heterogeneity. Further, the surface is flatter compared to 0.07 C. To conclude, increasing the charging rate yields a much more homogeneous film structure throughout the electrode compared to the slow film formation shown in the

previous section, because stochastic fluctuation could be reduced, while spatial differences remain moderate.

The dependency on electrode position is more distinct with higher C-rates, which is shown in Figure 10 for the same time as for 1 C formation. Here, close to the current collector, i.e., Figure 10 (A), SEI_3 components can barely be found. In contrast, at the other two positions, a SEI_3 rich region can be found at thicknesses larger than about 8 nm. Compared to 1 C formation, the fraction of SEI_1 is lower close to the separator and higher close to the current collector. Further, at 2 C discharge a peak of SEI_1 can be seen close to the surface. This peak is most distinct close to the current collector. Concerning statistical fluctuation of SEI_1 components, the trend shown with 1 C continues and yields statistically reproducible structures. Further, it can be seen that statistical fluctuations are higher close to the current collector. Moreover, significant deviations in thickness, composition and structure along the x coordinate can be seen.

The observed dependency between SEI composition and position x within the electrode can be assigned to macroscopic transport processes. In Figure 11, the concentration of lithium and solvent components along the x coordinate is shown for
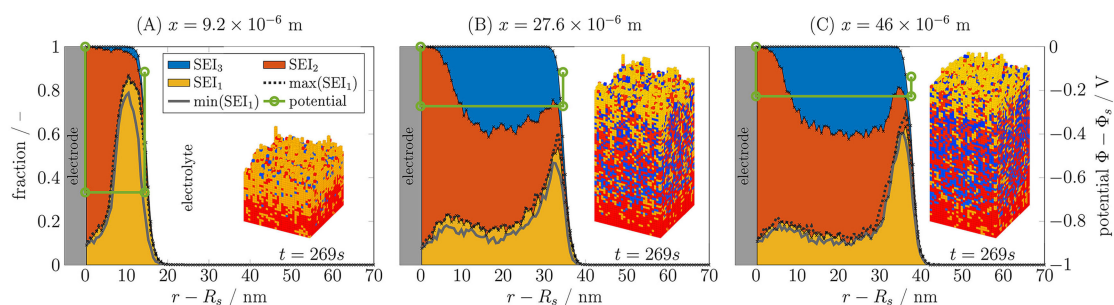

Figure 10. Composition and film structure of a kMC instance at $t = 269$ s during the first charge with 2 C at position $x = 9.2 \times 10^{-6}$ m (A), $x = 27.6 \times 10^{-6}$ m (B), and $x = 46 \times 10^{-6}$ m (C). For SEI_1 composition, also the maximum and minimum value out of four instances is shown. Further, electrode potential at electrode (s), left and right of film, and electrolyte (e) is shown.
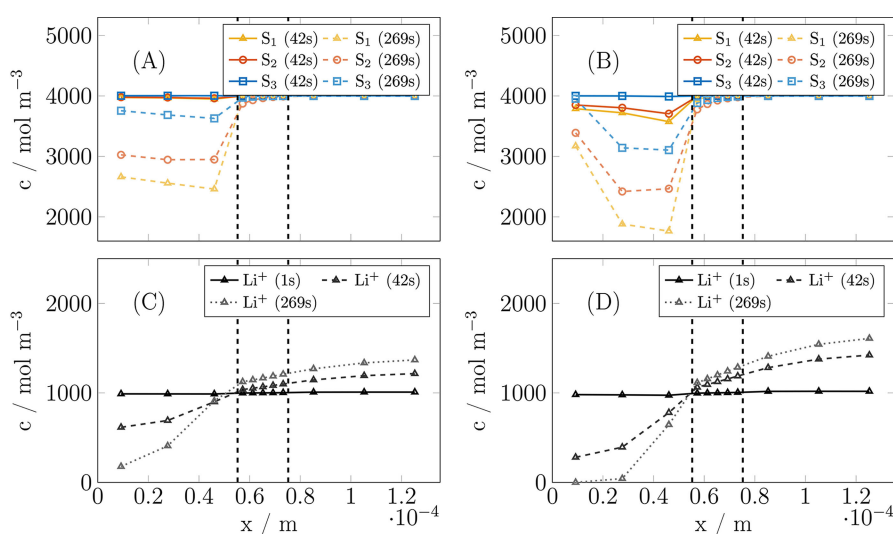

Figure 11. Spatial and temporal changes of concentration in the electrolyte for S_1, S_2, and S_3 (A) and concentration of Li^+ (C) for formation with 1 C. Concentration in the electrolyte for S_1, S_2, and S_3 (B) and concentration of Li^+ (D) at for formation with 2 C.

1 C and 2 C formation, respectively. Concentrations are shown at $t = 42$ s and $t = 269$ s. Comparing Figure 11 (A) and (B), it can be seen that with higher C-rates, solvent components are consumed significantly faster, which leads to lower concentrations and higher gradients along the x coordinate. This can be observed likewise for the concentration of lithium-ions, which is shown in Figure 9 (C) and (D). We note that lithium-ions are consumed by both, side reaction and lithium-intercalation. In Figure 9 and 10, the potential between solid and electrolyte is shown for various positions for 1 C and 2 C formation, respectively. Similar as has been observed with concentration gradients, potential gradients along the x coordinate increase with increasing C-rate. Comparing the trend in potential along x with the trend of film thickness reveals a strong correlation between both variables. Thereby, the significant difference in potential at 2 C can be assigned to high overpotentials at the electrolyte adsorption site due to depletion of lithium-ions in the electrolyte. As the macroscopic states, such as concentration and electrical potential, depend on x, and gradients increase with increasing C-rates, the input parameters from the kMC simulations also depend on x, which leads to the dependencies of composition and structure shown above.

In summary, the main observations for increasing the C-rate during film formation are as follows: (I) Fraction of SEI_1 components as well as the size of SEI_1 clusters decrease with increasing film growth rates; (II) Film structure is more homogeneous; (III) Dependency of film composition, structure, and thickness on the x coordinate increases. These findings indicate interaction throughout the scales, i.e., between the electrode and the atomistic scales. Based on the results shown in this section, in the following section the major aspects of the underlying processes and their multiscale interactions are outlined.

5.2. Discussion of the Multiscale Interaction

Increasing the C-rate enforces the increasing film growth rate, because more electrons need to be transferred at the interface. With this, mechanism 1 is disadvantaged compared to mechanism 2 and mechanism 3, which is explained in the following. With faster formation procedures, growing clusters of SEI_1 are rapidly covered by the other decomposition products. This denotes that there is not enough time for the SEI_1 clusters to establish, even though they are thermodynamically favored. A single microscopic process, which covers a SEI_1 component on the surface at the beginning of the film formation, may impede the growth of large clusters at this position and thus can significantly influence the development of the film locally. This explains the significant reduction of the SEI_1 fraction with increasing film growth rate. Moreover, this also explains the high heterogeneity and stochastic fluctuations for slow formation procedures.

If charging rates are very high, as for the simulation of a 2 C charge, concentrations and electrical potential depend significantly on distance to the current collector. Depletion of lithium-

ions close to the current collector leads to very low ionic conductivity and high overpotentials for lithium adsorption. Therefore, at this position the reaction rates at the surface are significantly reduced and yield a slower film growth rate. As slow growth favors SEI_1, this leads to gradient in fractions of SEI_1 along the x coordinates, higher fractions close to the current collector, due to slow film growth rate, and lower fractions close to the separator, due to high film growth rates. Moreover, as film growth slows down, SEI_1 clusters are formed on the surface at all positions. To conclude, with fast charging procedures, a significant difference in film structure and composition along the x coordinate can be observed.

The effects of the interaction observed here are strongly related to the heterogeneous mechanism and parameters we have chosen. However, it can be expected that a comparable interaction can be found with the actual decomposition mechanism, which is much more complex and most certainly heterogeneous as well, as batteries nowadays use a multi-component mixture of electrolytes which decompose differently.

In this paper, for the first time a distinct spatial and statistical distribution of film structure dependent on the applied current has been shown. We note that film thickness is mainly defined by the assumed leakage mechanisms as discussed in section 4.1. The leakage process was defined as homogeneous and structure independent, which would lead to equilibration of the thickness for cycling aging according to results shown with continuum models.[21] However, the simulated distribution of structural properties can not be simulated using continuum only models.

Aging of batteries is known to be caused by local heterogeneity,[10] thus the optimization of the film structure should aim for a homogeneous film throughout the electrode. The presented results indicate that local heterogeneity could be caused by both, too slow charging protocols, as stochastic effects prevail, and too fast charging protocols, causing spatial distributions. These findings suggest that there is an optimal charging rate for a certain electrolyte composition, and that today's state-of-the-art slow formation protocols can not necessarily be considered optimal for long life time. Another optimization objective could be to achieve certain optimal properties of the SEI, e.g., mechanical stability or high ionic conductivity. These are possibly related to the cluster size of certain SEI components, such as for the SEI_1 component of the example provided here. The presented results indicate that cluster size can be controlled by the charging procedure. Both suggested optimization tasks require consideration of the multiscale effects, as revealed in this article for the first time.

6. Conclusions

In this article, an extension of the P2D model by a heterogeneous surface film growth model using the kMC method was presented. The approach was used for an analysis of multiscale effects in lithium-ion batteries. Results illustrate multiscale interaction that can occur during formation protocols with low

and high C-rates. Results clearly reveal multiscale effects. With low charging rates, a strong impact of stochastic effects leads to a significant heterogeneity of film structure. With high charging rates, spatial distribution due to mass and charge transport on the electrode scale leads to strong dependency of film structure on position in the electrode.

The main parameters of the model were identified exemplarily by experimental data from electrochemical characterization of formation, OCP measurement, and C-rate tests. It was shown that the model can quantitatively describe the potential slope during the formation process. Further, the approach shows how a consistent model formulation and a step wise parameter identification can be applied. The identification of detailed model parameters for the atomistic model however would not be possible with the given experimental data. To refine parametreisation, reaction mechanisms and parameters of elementary steps in atomistic model should be calculated within future studies using DFT or MD simulations. The presented approach would allow to validate the mechanisms on macroscopic experiments. For detailed validation however, more experimental data should be involved. This can be realized for instance by measurement of generated gaseous species, e.g., using differential electrochemical mass spectrometer as shown for CO oxidation[44] and batteries,[45] or post mortem analysis of film composition.

With the presented results, we for the first time provide evidence for multiscale effects during molecular buildup of the SEI in lithium-ion batteries. We strongly recommend considering and researching such effects while optimizing formation procedures. A powerful methodology for multiscale analysis and optimization of this process is thereby provided with this article.

List of Symbols

Latin letters

a activity, –
a_s specific surface area, m^{-1}
A pre exponential factor, s^{-1}
A_e^{RK} Redlich Kister coefficient, –
c concentration, $mol\ m^{-3}$
C_{theo}^{As} theoretical capacity, $A\ s\ m^{-2}$
C^0 standard state concentration, $mol\ m^{-3}$
C^{DL} double layer capacitance, $F\ m^{-2}$
d^{film} film thickness, m
$\hat{d}^{film}$ local film thickness, m

D diffusion coefficient, $m^2\ s^{-1}$
E^A activation energy, $J\ mol^{-1}$
$\hat{E}^A$ specific activation energy, $J\ mol^{-1}\ m^{-1}$
F   Faraday constant, $A\ s\ mol^{-1}$
I_{cell} applied current, $A\ m^{-2}$
j current density, $A\ m^{-3}$
J microscopic process, –
k^f forward reaction rate constant, s^{-1}

k^b backward reaction rate constant, s^{-1}
N_s site density, m^{-2}
o_s site occupancy number, mol^{-1}
p probability,
q flux, $mol\ m^{-2}\ s^{-1}$
r_s roughness factor, –
R   ideal gas constant, $J\ mol^{-1}\ K^{-1}$
r radial space variable, m
R^{film} specific electrical film resistance, $\Omega\ m$
R_s particle radius, m
t time, s
t_p transference number, –
T temperature, K
x electrode space variable, m
x^{Li} interacalation fraction, –

Greek letters

β symmetry factor, –
δ thickness, m
ΔG^0 standard state Gibbs free energy, $J\ mol^{-1}$
$\Delta \Phi$ electrical potential difference, V
Δt time difference, s
Γ microscopic rate, s^{-1}
θ surface fraction, –
$\vartheta^{lattice}$ lattice site state, –
ϑ^{film} film site state, –
ε volume fraction, –
μ^0 standard state chemical potential, $J\ mol^{-1}$
Φ electrical potential, V
σ electrical conductivity, $S\ m^{-1}$
σ_{De} diffusional ionic transport coefficient, $V\ S\ m^{-1}$
τ tortuosity, –

Conflict of Interest

The authors declare no conflict of interest.

[1] S. J. An, J. Li, C. Daniel, D. Mohanty, S. Nagpure, D. L. Wood, *Carbon* **2016**, *105*, 52 76.
[2] W. Märkle, C. Y. Lu, P. Novák, *J. Electrochem. Soc.* **2011**, *158*, A1478 A1482.
[3] F. German, A. Hintennach, A. LaCroix, D. Thiemig, S. Oswald, F. Scheiba, M. J. Hoffmann, H. Ehrenberg, *J. Power Sources* **2014**, *264*, 100 107.

[4] B. K. Antonopoulos, F. Maglia, F. Schmidt Stein, J. P. Schmidt, H. E. Hoster, *Batteries* **2018**, *1*, 1 13.

[5] V. A. Agubra, J. W. Fergus, *J. Power Sources* **2014**, *268*, 153 162.

[6] E. Peled, D. Golodnitsky, G. Ardel, *J. Electrochem. Soc.* **1997**, *144*, L208 L210.

[7] E. Peled, D. Bar Tow, A. Merson, A. Gladkich, L. Burstein, D. Golodnitsky, *J. Power Sources* **2001**, *97 98*, 52 57.

[8] S. Chattopadhyay, A. L. Lipson, H. J. Karmel, J. D. Emery, T. T. Fister, P. A. Fenter, M. C. Hersam, M. J. Bedzyk, *Chem. Mater.* **2012**, *24*, 3038 3043.

[9] S. Bertolini, P. B. Balbuena, *J. Phys. Chem. C* **2018**, *122*, 10783 10791.

[10] S. J. Harris, P. Lu, *J. Phys. Chem. C* **2013**, *117*, 6481 6492.

[11] T. C. Bach, S. F. Schuster, E. Fleder, J. Müller, M. J. Brand, H. Lorrmann, A. Jossen, G. Sextl, *J. Energy Storage* **2016**, *5*, 212 223.

[12] M. Safari, C. Delacourt, *J. Electrochem. Soc.* **2011**, *158*, A1436 A1447.

[13] A. M. Colclasure, K. A. Smith, R. J. Kee, *Electrochim. Acta* **2011**, *58*, 33 43.

[14] F. Hao, Z. Liu, P. B. Balbuena, P. P. Mukherjee, *J. Phys. Chem. C* **2017**, *121*, 26233 26240.

[15] R. N. Methekar, P. W. C. Northrop, K. Chen, R. D. Braatz, V. R. Subrama nian, *J. Electrochem. Soc.* **2011**, *158*, A363 A370.

[16] J. Vatamanu, O. Borodin, G. D. Smith, *J. Phys. Chem.* **2012**, *116*, 1114 1121.

[17] P. Ganesh, P. R. C. Kent, D. Jiang, *J. Phys. Chem. C* **2012**, *116*, 24476 24481.

[18] K. Leung, J. L. Budzien, *Phys. Chem. Chem. Phys.* **2010**, *12*, 6583 6586.

[19] D. Bedrov, G. D. Smith, A. C. T. Van Duin, *J. Phys. Chem. A* **2012**, *116*, 2978 2985.

[20] M. T. Lawder, P. W. C. Northrop, V. R. Subramanian, *J. Electrochem. Soc.* **2014**, *161*, A2099 A2108.

[21] M. B. Pinson, M. Z. Bazant, *J. Electrochem. Soc.* **2013**, *160*, A243 A250.

[22] A. A. Tahmasbi, T. Kadyk, M. H. Eikerling, *J. Electrochem. Soc.* **2017**, *164*, A1307 A1313.

[23] F. Single, A. Latz, B. Horstmann, *ChemSusChem* **2018**, *11*, 1950 1955.

[24] M. Tang, S. Lu, J. Newman, *J. Electrochem. Soc.* **2012**, *159*, A1775 A1785.

[25] A. A. Franco, *RSC Adv.* **2013**, *3*, 13027 1305.

[26] M. A. Quiroga, K. Malek, A. A. Franco, *J. Electrochem. Soc.* **2016**, *163*, F59 F70.

[27] M. A. Quiroga, A. A. Franco, *J. Electrochem. Soc.* **2015**, *162*, E73 E83.

[28] F. Roder, R. D. Braatz, U. Krewer, *Comput. Chem. Eng.* **2019**, *121*, 722 735.

[29] F. Röder, R. D. Braatz, U. Krewer, *J. Electrochem. Soc.* **2017**, *164*, E3335 E3344.

[30] C. Shinagawa, H. Ushiyama, K. Yamashita, *J. Electrochem. Soc.* **2017**, *164*, A3018 A3024.

[31] M. Doyle, T. F. Fuller, J. Newman, *J. Electrochem. Soc.* **1993**, *140*, 1526 1533.

[32] N. Legrand, S. Raël, B. Knosp, M. Hinaje, P. Desprez, F. Lapicque, *J. Power Sources* **2014**, *251*, 370 378.

[33] M. Schleutker, J. Bahner, C. L. Tsai, D. Stolten, C. Korte, *Phys. Chem. Chem. Phys.* **2017**, *19*, 26596 26605.

[34] A. M. Colclasure, R. J. Kee, *Electrochim. Acta* **2010**, *55*, 8960 8973.

[35] G. Sikha, B. N. Popov, R. E. White, *J. Electrochem. Soc.* **2004**, *151*, A1104 A1114.

[36] E. J. Plichta, W. K. Behl, *J. Power Sources* **2000**, 88, 192 196.

[37] M. Doyle, J. Newman, A. S. Gozdz, C. N. Schmutz, J. M. Tarascon, *J. Electrochem. Soc.* **1996**, *143*, 1890 1903.

[38] F. Single, B. Horstmann, A. Latz, *Phys. Chem. Chem. Phys.* **2016**, *18*, 17810 17814.

[39] D. Li, D. Danilov, Z. Zhang, H. Chen, Y. Yang, P. H. L. Notten, *J. Electrochem. Soc.* **2015**, *162*, A858 A869.

[40] A. Chatterjee, D. G. Vlachos, *J. Comput. Aided Mater. Des.* **2007**, *14*, 253 308.

[41] E. Peled, D. Golodnitsky, C. Menachem, D. Bar Tow, *J. Electrochem. Soc.* **1998**, *145*, 3482 3486.

[42] D. Goers, M. E. Spahr, A. Leone, W. Märkle, P. Novák, *Electrochim. Acta* **2011**, *56*, 3799 3808.

[43] M. Q. Xu, W. S. Li, X. X. Zuo, J. S. Liu, X. Xu, *J. Power Sources* **2007**, *174*, 705 710.

[44] F. Kubannek, U. Krewer, *Electrochim. Acta* **2016**, *210*, 862 873.

[45] B. B. Berkes, A. Jozwiuk, H. Sommer, T. Brezesinski, J. Janek, *Electrochem. Commun.* **2015**, *60*, 64 69.